Interatomic potential for germanium dioxide empirically fitted to an *ab initio* energy surface

R. D. Oeffner and S. R. Elliott
Department of Chemistry, University of Cambridge, Lensfield Road, Cambridge CB2 1EW, United Kingdom
(Received 3 December 1997; revised manuscript received 12 June 1998)

We have developed a two-body potential for GeO_2 which we employ for modeling the α-quartz and the rutilelike phases of GeO_2. In simulations both at ambient and at elevated pressure, the bond angles and bond lengths agree well with experimental values. The vibrational spectra have been analyzed both from the harmonic approximation and from velocity autocorrelation functions. The limits of the harmonic approximation are demonstrated with a method called selective molecular-dynamics simulation. The α- to β-quartz phase transition is successfully modeled. [S0163-1829(98)03542-5]

I. INTRODUCTION

The incentive to carry out calculations with potentials founded on first principles has led to various approaches. In recent years a significant amount of work has been done on *ab initio* molecular-dynamics (MD) simulations.[1–3] The ever increasing computer speed gradually has made such calculations possible now also on smaller workstations; the limit of the system size for such simulations is today typically below 100 atoms or so, making it unfeasible to study any effects that occur at distances greater than a few Ångströms. *Ab initio* MD simulations are therefore currently precluded for the study of bulk properties of solids and liquids. One way to tackle this problem is therefore to map the potential energy surface for various configurations of some carefully selected cluster of atoms from the system and then perform a fit of a suitable interatomic potential to this energy surface, hoping that such a potential will prove successful in classical molecular-dynamics simulations. Over the past decade, interatomic potentials for a wide range of compounds have been developed with such methods.[4,5] It is to be addressed exactly what is meant by the term ''a suitable potential.'' The functional form of interatomic potentials, and of pair potentials in particular, has in a substantial amount of work been assumed to have an intuitively comprehensible analytical form, e.g., electrostatics plus an exponentially decaying short-range repulsion. Such expressions can of course be justified for ionic solids,[6,7] but are seriously at odds with what are suitable potentials for modeling metals or covalent bonds in general. As has been demonstrated,[8,9] metal potentials can be successfully modeled with a pair-functional form. Carlsson *et al.*[10] pioneered a procedure on how to invert the cohesive energy into a pair potential. This method was recently improved by Bazant and Kaxiras[11] who generalized the method to work for many-body potentials. They demonstrate furthermore how the functional form of angle-dependent three-body forces for silicon, the Stillinger-Weber expression,[12] can be optimized and thus arrive at a functional three-body form which differs significantly from the original Stillinger-Weber potential. The functional form of Bazant's potential is likely to be a good candidate when attempting to explain the physical significance of the various terms in their potential for silicon. Thus when developing interatomic potentials, one should first investigate what is a suitable functional form for the interatomic potentials and after that proceed by fitting the potential parameters to energy databases, bulk information, etc. Following the success of Tsuneyuki[4] and other workers[13] who used pair potentials of the Buckingham form for the description of SiO_2, we adopt the same functional form of the pair potential for GeO_2 that we develop.

Germanium dioxide is particularly interesting to study because it is similar to silicon dioxide in many respects. Both compounds can exist in α as well as β-quartz phases.[14] Strictly speaking, the α-quartz form of GeO_2 is a metastable phase that can be obtained by cooling the β-quartz phase of GeO_2 below 1020 °C. The β-quartz phase of GeO_2 is thermodynamically stable only above 1049 °C. Below this temperature the stable phase is an octahedral rutilelike phase. But as the phase change is sluggish it turns out to be easy to quench it to the α-quartz phase of GeO_2 by supercooling it. The α-quartz phase of germanium dioxide is much less inert than its silicon cousin, and is even soluble in water.[14] The octahedral rutilelike phase of silica, stishovite, is stable[15] above approximately 70 GPa, whereas the rutile phase of GeO_2 is stable even at ambient pressure. Phase transitions between two crystalline phases of very different symmetry (i.e., change in the coordination numbers of the involved atoms) at ambient pressure triggered only by a temperature change traditionally pose a severe challenge to model with simple potentials. Although success has been made[16,17] in modeling phase transitions in various compounds, such phase transitions are of the soft-mode type and do not involve bond breaking. Work[18] carried out in modeling the phase transition of both phases of GeO_2 with the same interatomic potential used computationally expensive three-body potentials and the results are somewhat tentative. Very recently, Tsuchiya *et al.*[19] have presented a pair potential that successfully models both phases of GeO_2, but this potential fails to predict the dynamical properties properly. The achievement of a pair potential for GeO_2 is therefore still a fruitful area for study which is our motivation for the work presented here.

A significant structural parameter when modeling germania in the α-quartz phase is to achieve the correct Ge-O-Ge bond angle of 130°. Because the angle is not as obtuse as in, say silica, it has been thought difficult to model without introducing many-body terms since the positively charged Ge atoms should repel each other, thus enlarging the oxygen

bond angle. This corresponds to an ionic model of the atomic interactions. However, because the electrons are less localized in GeO_2 than in a completely ionic solid, a more covalent description will be better. To a first approximation this entails partial charges on the species involved.

In this work we follow the idea, applied by Tsuneyuki *et al.*[4] for SiO_2, of deriving an interatomic potential for GeO_2 by fitting the potential parameters to a potential energy surface for a $Ge(OH)_4$ cluster calculated with a Hartree-Fock program. We then demonstrate that both the α-quartz GeO_2 and the rutilelike GeO_2 crystal are stable with this potential in molecular-dynamics simulations. Next we analyze the vibrational properties both in the harmonic approximation and from the velocity autocorrelation function obtained from the MD simulations. The validity of the harmonic approximation is assessed with the aid of selective molecular-dynamics simulations. Finally we demonstrate the existence of the α to β-quartz phase transition. The potential we chose is a two-body potential of the Buckingham type. A more sophisticated model with higher-order terms in the potential model would possibly be less transferable[20] to other systems, which justifies resorting to a simple potential model.

II. THEORY

As in Refs. 4 and 13, we calculate a potential energy surface for a $Ge(OH)_4$ cluster by bending, twisting, and stretching the GeO bonds. The modes considered were the ones that preserve T_d, C_{3v}, and D_{2d} symmetries. It is believed that such a potential energy surface may represent a subset of the true multidimensional potential energy surface experienced by a GeO_4 entity in the bulk of the quartz crystal, at least up to a more-or-less arbitrary additive energy constant. Whereas in Refs. 4,13 the potential energy surface was mapped along each of these three symmetry modes only, we calculated instead the energy for the different configurations of the cluster by simultaneously moving along these three modes. Thus in our work only the C_2 symmetry of the $Ge(OH)_4$ cluster is preserved. We thereby obtain a four-dimensional energy surface as opposed to the three one-dimensional energy surfaces obtained by Tsuneyuki. It is believed that this extra information should improve the quality of the final interatomic potential. As the cluster is small, there is no significant computational cost in doing this. Furthermore, as we sample a greater subset of the true multidimensional potential energy surface, we can infer that any fitting of interatomic potential parameters to this more extensive potential energy surface will be more accurate than had we only used the one-dimensional energy surfaces.

The idea of using a tetrahedral $Ge(OH)_4$ cluster rather than an octahedral GeO_6 cluster as the primary entity for deriving a potential energy surface is convenient for the following reasons. It is known that not only in the α quartz but also in the vitreous phase the Ge atoms are four-coordinated, i.e., tetrahedrally linked to oxygen atoms. A potential derived from a similar environment is therefore likely to be more transferable than one derived only for the rutile phase. It is worth stressing that, even though the potential parameters are fitted to a potential energy surface derived from first principles, such a fit serves only as a suitable starting point when constructing the final parameter set. Empirical information, like elastic constants or vibrational spectra also has to be considered as will be demonstrated.

A. *Ab initio* calculations

The Hartree-Fock program, CADPAC,[21] which is simple to use and is readily available as a source code for many different types of computers, was the program used to calculate the energy surface.

When doing Hartree-Fock calculations it has long been recognized[22] that there is no unique choice of basis-set functions even for small systems. The basis set we chose was augmented with *d*-orbital-like functions in order to model better any polarizability effects on the oxygen atoms. We made a compromise between the 6-31G* and the more crude STO-3G basis sets as the former seemed too computationally expensive in test calculations. We thus arrived at the 3-21G* basis set which is available for oxygen but has not yet been officially defined for germanium. We composed a 3-21G* basis set for germanium by adding a *d*-type orbital to the 3-21G basis that has been defined for germanium. A contraction coefficient of 1 and a contraction exponent of 0.432 for the *d*-type orbital was found to be fairly optimal when calculating the self-consistent field (SCF) energy of a single germanium atom.

The SCF potential energy surface for the $Ge(OH)_4$ cluster was then calculated by repetitive SCF calculations retaining only the C_2 symmetry of the cluster. The Ge-O bond distance was varied between 0.8 and 2.6 Å. Between 1.5 and 1.9 Å the sampling was denser as we anticipate the equilibrium configuration to be found there and the fitting algorithm described below will benefit from more information in that range. The calculations sampled five O-Ge-O bond angles ranging (we made sure to sample the ideal tetrahedral angle 109.47° as well) from approximately $\theta = 86°$ to $\theta = 180°$. Thus, the 180° configuration corresponds to the planar configuration where the Ge atom is surrounded by the oxygen atoms.

The purpose of the hydrogen atoms is to neutralize the charge of the whole cluster. That is, we omit any electron wave functions on the hydrogen atoms but demand that the cluster as a whole should be electrically neutral. The hydrogens (or positive unit charges as they really are) are fixed onto the Ge-O vectors at a constant distance from the respective oxygen atoms throughout the repetitive displacements of oxygen atoms during the SCF calculations. The H-O distance was chosen to be 1.73 Å in anticipation that this would reflect equilibrium geometries in the bulk in the best possible manner, as this is very close to the experimental Ge-O distance observed in tetrahedrally coordinated environments.

B. Fitting algorithm

The potential we used is a pair potential of the Buckingham type:

$$V(r_{ij}) = \frac{Z_i Z_j}{4\pi\epsilon_0 r_{ij}} + A_{ij} e^{-r_{ij}/\rho_{ij}} - \frac{C_{ij}}{r_{ij}^6}. \qquad (1)$$

The parameters of the pair potential were fitted to the energies obtained from the SCF calculations with the aid of the

TABLE I. Potential parameters obtained from the *ab initio* energy surface.

	A_{ij} in kJ/mol	ρ_{ij} in Å	C_{ij} in kJ/(Å^6 mol)
Original fitted potential			
Ge,O	2.00696×10^7	0.16315	22833
O,O	7.42295×10^5	0.304404	12648
$Z_{Ge}=-2Z_O=1.5e$			
Rescaled potential			
Ge,O	7.9108×10^6	0.16315	9000
O,O	2.9259×10^5	0.304404	4985
$Z_{Ge}=-2Z_O=0.94174e$			

Levenberg-Marquardt[23] algorithm. This algorithm, based on a nonlinear least-squares fit, requires weights to be assigned to each of the data entries used for fitting, where a large weight plays down the importance of the respective data entry. The objective is to minimize

$$\chi^2(\mathbf{a})=\sum_{i=1}^{N}\left[\frac{E_i^{\mathrm{SCF}}-E_i(\mathbf{a})}{\sigma_i}\right]^2 \tag{2}$$

in parameter space, where **a** is the vector of potential parameters in Eq. (1), $E_i(\mathbf{a})$ is the potential energy of the ith atomic configuration as a function of the potential parameters in Eq. (1), N is the number of atomic configurations and σ_i is the weight assigned to the ith configuration. Again we anticipated that those configurations far away from the equilibrium configuration of an ideal tetrahedron in the bulk will not be of great importance when fitting the interatomic potential parameters to the SCF energy surface. In other words, it does not matter if the interatomic potential we arrive at is only approximately correct for configurations far away from equilibrium as these configurations possibly would only rarely be attained in a molecular-dynamics simulation. Therefore, we assigned small weights for configurations close to equilibrium geometries. By sorting the data entries in ascending order with respect to the calculated SCF energies, the equilibrium structure of the cluster was identified as the regular tetrahedron with a Ge-O distance close to the observed equilibrium distance of Ge-O in the α-quartz form of germanium dioxide. The weights were then gradually increased for configurations with increasing energies.

An ambiguity arises when defining the short-range parameters for the germanium atom. Strictly speaking it is undefined as there is no other Ge atom with which to interact in the SCF calculations. Only the electrostatic charge ensures that two germanium atoms will not coincide during a molecular-dynamics simulation. On the other hand, it may well be that in order to obtain a correct Ge-O-Ge bond angle, Ge-Ge interactions should not be ignored.

When fitting the parameters A_{GeO}, A_{OO}, ρ_{GeO}, ρ_{OO}, C_{GeO}, and C_{OO} in Eq. (1), the charges on the atoms were held fixed. The values of the charges were determined from the Mulliken charge population analysis in SCF calculations for the believed equilibrium geometry of a tetrahedral $Ge(OH)_4$ cluster, i.e., a regular tetrahedron with a Ge-O bond distance of 1.74 Å. The resultant partial charges on germanium and oxygen in this SCF calculation proved to be very sensitive to the particular choice of basis sets and one should therefore not attach too much meaning to the charge values.

The parameters from the Tsuneyuki[4] potential serve as a good initial guess for the fitting algorithm because of the similarities between α-quartz silica and germania. Possibly $\chi(\mathbf{a})$ in Eq. (2) will have many local minima in the parameter space to which the algorithm will eventually arrive. In other words, an optimal value of **a** is not necessarily unique for a particular SCF energy surface. So, for each different initial guess for the parameters, the algorithm is therefore likely to end up in a correspondingly different local minimum in parameter space, when fitting to the same SCF energy surface. This amounts to saying that the procedure of assigning weights to the SCF energies and even choosing which are the SCF energies of interest, is inherently empirical in nature. We found it necessary to generate some hundred potentials where we had ''experimented'' with the assigned weights. Each of these potentials was then tested as described below.

III. MOLECULAR-DYNAMICS SIMULATIONS

Whether a resultant potential is of good quality or not can be assessed by molecular-dynamics simulations. We used the N-P-T ensemble for these simulations, together with an anisotropic barostat that allows strain fluctuations as well as the size of the simulation cell to change. The pressure tensor was set to zero. The potentials were tested in MD simulations on an ideal α-quartz GeO_2 structure, the details of which are given in the Appendix. From those parameters we chose the potentials that modeled the α-quartz GeO_2 structure the best, i.e., reproduced the characteristic bond lengths and bond angles the best. We thereby reduced the hundreds of potentials generated from the fitting procedure to a more manageable number of about 20 sets of potential parameters that all yielded stable α-quartz GeO_2 structures. Each of those sets of parameters were subsequently tested in MD simulations of the rutilelike GeO_2 structure to identify which of those potentials might also stabilize this crystalline phase. These calculations were also done with the N-P-T ensemble under zero stress and pressure. As a result we arrived at a set of parameters that were capable of stabilizing both crystal phases, see Table I.

A. Spectra within the harmonic approximation

In the harmonic limit, the potential energy is expanded around the equilibrium position of the atoms to second order in the atomic coordinates,

$$U(\mathbf{r}) = U(\mathbf{r}_0) + \frac{1}{2}\mathbf{r}^t \mathbf{H}(\mathbf{r}_0)\mathbf{r}, \tag{3}$$

where $\mathbf{r}$ is a $3N$-dimensional vector with Cartesian coordinates of the N atoms in the system, $\mathbf{r}_0$ is the equilibrium position, i.e., a local minimum of U and t indicates the transpose. $\mathbf{H}(\mathbf{r}_0)$ is given as the mass-weighted second derivative matrix:

$$\mathbf{H}(\mathbf{r}^0)_{i,j,\alpha,\beta} = \frac{1}{\sqrt{m_i m_j}} \frac{\partial^2 U(\mathbf{r}^0)}{\partial \mathbf{r}_{i,\alpha} \partial \mathbf{r}_{j,\beta}}, \tag{4}$$

where $\mathbf{r}_{i,\alpha}$ is the Cartesian component α of the coordinate vector for atom i and m_i is its mass. Its interpretation is as follows. When moving the ith atom along the Cartesian component α, a change in the Cartesian component β of the force on the jth atom occurs. As we consider U to be composed of a sum of the pair potentials given in Eq. (1), $U(\mathbf{r}) = \frac{1}{2}\Sigma_{i,j}^{N} V(r_{ij})$, the mass-weighted second derivative matrix becomes

$$\mathbf{H}(\mathbf{r}_0)_{i,j,\alpha,\beta} = \begin{cases} \dfrac{1}{\sqrt{m_i m_j}} \dfrac{\partial^2 V(r_{ij}^0)}{\partial \mathbf{r}_{i,\alpha} \partial \mathbf{r}_{j,\beta}}, & i \neq j \\ \displaystyle\sum_{k \neq i}^{N} \dfrac{-1}{\sqrt{m_i m_k}} \dfrac{\partial^2 V(r_{ik}^0)}{\partial \mathbf{r}_{i,\alpha} \partial \mathbf{r}_{k,\beta}}, & i = j, \end{cases} \tag{5}$$

where r_{ij}^0 is the vector separating atom i from j for the equilibrium configuration $\mathbf{r}^0$.

If the system is set up with periodic boundary conditions, the angular momentum is not a constant of motion and diagonalization of $\mathbf{H}(\mathbf{r_0})$ yields $3N-3$ force constants differing from zero. The square roots of these force constants then correspond to the vibrational frequencies of the associated normal-mode eigenvectors. The vibrational density of states (VDOS) is calculated as a histogram of these discrete frequencies convoluted with some smooth function to obtain definite linewidths of size h when plotting the VDOS(ω),

$$\mathrm{VDOS}(\omega) = \sum_{j=1}^{3N-3} g(\omega - \omega_j, h). \tag{6}$$

We chose $g(\omega,h)$ to be a Gaussian with a half width h of 1 THz.

The infrared intensity of mode ω_j is calculated as being equal to the square of the fluctuations in the dipole moment,

$$I_{\omega_j} = (\Delta \mu_{\omega_j})^2, \tag{7}$$

where

$$\Delta \mu_{\omega_j} = \sum_{i=1}^{N} q_i \mathbf{d}_i^{\omega_j}, \tag{8}$$

q_i being the charge of atom i and where $\mathbf{d}_i^{\omega_j}$ is the Cartesian vector component of the displacement eigenvector, i.e., mass-weighted normal-mode eigenvector for atom i at normal-mode frequency ω_j. Although there exist other ways[24,25] of calculating the infrared spectra, the above method is by far the simplest and easiest to implement.

For predicting the Raman spectra we employed the bond-polarizability model by Long,[26] and used the implementation given by Creighton *et al.*[27] In this model, the overall polarizability tensor of the system is a sum of individual bond polarizabilities

$$\boldsymbol{A}_{\mu\nu} = \sum_{i<j} \boldsymbol{\alpha}_{\mu\nu}(r_{ij}), \tag{9}$$

where μ,ν are Cartesian components x,y,z and i,j indicates the bond from atom i to atom j. In the case of cylindrically symmetric bonds, the individual bond polarizabilities in this model can be shown to be[27]

$$\boldsymbol{\alpha}_{\mu\nu}(r_{ij}) = \alpha_{ij}^{\perp}\delta_{\mu\nu} + (\alpha_{ij}^{\parallel} - \alpha_{ij}^{\perp})\,\eta_{ij\mu}\eta_{ij\nu}, \tag{10}$$

where the parallel and perpendicular bond polarizabilities, $\alpha_{ij}^{\parallel}$ and $\alpha_{ij}^{\perp}$ are assumed to depend on the bond length $|r_{ij}|$ only, and $\eta_{ij\mu}$ is the direction cosine between bond ij and the Cartesian axis μ. To make the dependence of $|r_{ij}|$ explicit, it is assumed that $\boldsymbol{\alpha}_{\mu\nu}$ depends on the length of r_{ij} in the following fashion:

$$\boldsymbol{\alpha}_{\mu\nu}(r_{ij}) = [\alpha_{ij}'^{\perp}\delta_{\mu\nu} + (\alpha_{ij}'^{\parallel} - \alpha_{ij}'^{\perp})\,\eta_{ij\mu}\eta_{ij\nu}]|r_{ij}|. \tag{11}$$

The values of $\alpha_{ij}'^{\parallel}$ and $\alpha_{ij}'^{\perp}$ are then the input to the program.

For calculating the Raman intensity of mode ω in the harmonic approximation we require the change in the overall polarizability tensor with respect to the vibrational mode ω:

$$\boldsymbol{A}'_{\omega,\mu\nu} = \sum_{i<j} \boldsymbol{\alpha}'_{\mu\nu}(r_{ij}^{\omega}), \tag{12}$$

where we define the derivative of the bond polarizability with respect to the vibrational mode ω as

$$\boldsymbol{\alpha}'_{\mu\nu}(r_{ij}^{\omega}) = \frac{\boldsymbol{\alpha}_{\mu\nu}(r_{ij} + \Delta r_{ij}^{\omega}) - \boldsymbol{\alpha}_{\mu\nu}(r_{ij} - \Delta r_{ij}^{\omega})}{|\Delta r_{ij}^{\omega}|}. \tag{13}$$

Here Δr_{ij}^{ω} is a finite differential bond-change vector obtained by subtracting the displacement vector on atom j from the displacement vector on atom i, both at normal-mode frequency ω. Thus, Δr_{ij}^{ω} is the change in the bond vector for normal-mode ω. The square of each of the nine components of $\boldsymbol{A}'_{\omega}$ then corresponds to Raman scattering in the respective directions; i.e., if $\boldsymbol{A}'_{\omega,\mu\nu}$ is nonzero, this means that incident electromagnetic radiation with the electrical field vector polarized along the μ axis will give rise to scattered radiation with the electrical field vector polarized along the ν axis. The change in the mean polarizability,

$$a'_{\omega} = \frac{1}{3}(\boldsymbol{A}'_{\omega,xx} + \boldsymbol{A}'_{\omega,yy} + \boldsymbol{A}'_{\omega,zz}), \tag{14}$$

and the change in the anisotropy,

$$\gamma'^{2}_{\omega}=\frac{1}{2}[(\boldsymbol{A}'_{\omega,xx}-\boldsymbol{A}'_{\omega,yy})^2+(\boldsymbol{A}'_{\omega,yy}-\boldsymbol{A}'_{\omega,zz})^2 +(\boldsymbol{A}'_{\omega,zz}-\boldsymbol{A}'_{\omega,xx})^2+6(\boldsymbol{A}'^{2}_{\omega,xy}+\boldsymbol{A}'^{2}_{\omega,yz}+\boldsymbol{A}'^{2}_{\omega,zx})], \tag{15}$$

remain invariant when rotating the system. The spherically averaged intensity can then be shown to be[26]

$$I(\omega)=\frac{45a'^{2}_{\omega}+4\gamma'^{2}_{\omega}}{45}. \tag{16}$$

This quantity is relevant for gases, amorphous solids, liquids and crystal powders and is the one we used for predicting the Raman spectrum. To our knowledge there are no data for the bond polarizabilities of α-quartz GeO_2 in the literature. We thus performed two SCF calculations on the $Ge(OH)_4$ cluster. One was set up as an ideal tetrahedron with all GeO bond lengths equal to 1.74 Å and one where one of the GeO bonds was stretched a bit, say, to 1.76 Å. Subtracting the polarizability tensors obtained from these two configurations then gives the change in the polarizability tensor as a function of bond-length change. In the case where the GeO bond to be stretched is aligned parallel with the x axis, $\alpha^{\parallel}_{\mathrm{GeO}}$ can be identified as α_{xx} and $\alpha^{\perp}_{\mathrm{GeO}}$ can be identified as $\alpha_{yy}=\alpha_{zz}$. For these calculations we employed the basis-set 6311G* on the oxygen and germanium atoms[28] as the larger number of d and p orbitals in this basis set are more suitable for studies of polarization effects. These calculations were done at MP2 level. We found that $\alpha'^{\parallel}_{\mathrm{GeO}}=2.79$ Å^2 and $\alpha'^{\perp}_{\mathrm{GeO}}=0.41$ Å^2. These values, however, poorly reproduced the Raman spectrum and instead we resorted to using *ad hoc* values with $\alpha'^{\parallel}_{\mathrm{GeO}}=2.79$ Å^2 and $\alpha'^{\perp}_{\mathrm{GeO}}=1.67$ Å^2. Although this is, in principle, unsatisfactory it has been done previously in simulations of Raman spectra.[27] The poor agreement with the *ab initio* values for $\alpha'^{\parallel}_{\mathrm{GeO}}$ and $\alpha'^{\perp}_{\mathrm{GeO}}$ may be due to the fact that single cluster calculations are not suitable in predicting higher-order electrostatic properties like polarizability tensors for the bulk. We have not pursued this issue further. For completeness, one could also assign bond-polarizability derivatives for the bonds OO and GeGe although this has no significance as the interatomic distances between these pairs of atoms always exceed what is defined as the maximum bond length for such pairs. For the calculation of the infrared spectra, we used the partial charges given in Table I. Finally we convoluted both the infrared intensity histogram and the Raman histogram with a Gaussian function as in Eq. (6).

B. Projection of normal modes onto symmetry modes of structural units

The structural units studied here are the Ge-O-Ge and the GeO_4 units. In silica the corresponding SiOSi and SiO_4 units provide a good understanding of the dynamics of silica[29,30] which we believe also will be the case for the Ge-O-Ge and the GeO_4 units in GeO_2.

The way we analyzed the projection of the normal modes onto symmetry modes is as follows. For each Ge-O-Ge or GeO_4 unit, we constructed the 6 or 12 symmetry modes, respectively. The symmetry modes for a Ge-O-Ge unit consist of one symmetric-stretching mode, one asymmetric-stretching mode, two or one bending modes and two or three rotational modes, depending on whether the Ge-O-Ge unit is linear or not, respectively. The symmetry modes for the tetrahedron consist of two symmetric bending modes, one symmetric-stretching mode, three asymmetric-stretching modes, three asymmetric-bending modes plus three rotational modes, see Fig. 1. The modes are then Gram-Schmidt orthonormalized with respect to each other. This makes sense for the tetrahedral units which are quite distorted from an ideal tetrahedron and for the Ge-O-Ge units which in general have a wide range of Ge-O-Ge angles. Retaining ideal symmetry modes for distorted tetrahedra may result in some of the ideal symmetry modes mixing with one another which would give rise to a more ambiguous mode assignment. Usually it is still possible to classify these new orthonormal symmetry modes as members of the particular symmetry species, F_2, A_1, etc. These new orthonormal symmetry modes were then projected onto each of the normal modes obtained from the Hessian diagonalization. For instance, the projection of the symmetry mode i onto normal mode ω for some Ge-O-Ge unit is calculated as follows:

$$c_i^{\omega}=\begin{pmatrix}\mathbf{0}\\ \mathbf{0}\\ \vdots\\ \mathbf{u}_{is}\\ \mathbf{u}_{it}\\ \mathbf{u}_{iu}\\ \mathbf{0}\\ \vdots\end{pmatrix}\cdot\begin{pmatrix}\mathbf{n}_1^{\omega}\\ \mathbf{n}_2^{\omega}\\ \vdots\\ \\ \\ \\ \vdots\\ \mathbf{n}_N^{\omega}\end{pmatrix}, \tag{17}$$

where s, t, and u are indices for the germanium and oxygen atoms. Before calculating c_i^{ω}, we transformed both $\mathbf{u}_i$ and $\mathbf{n}^{\omega}$ to the center-of-mass frame of the atomic cluster considered in $\mathbf{u}_i$. The above procedure is performed for all Ge-O-Ge and GeO_4 units and a histogram of $|c_i^{\omega}|^2$ was then constructed with the normal-mode frequencies labeling each bin. Details of the calculations are given in the Appendix.

C. Spectra obtained from autocorrelation functions

Calculation of the velocity autocorrelation function is another conventional method[31–34] of obtaining the VDOS. For obtaining the VDOS, the mass-weighted velocity autocorrelation function is Fourier transformed;

$$\mathrm{VDOS}(\omega)=\frac{1}{\sqrt{2\pi}}\int C_M(t)e^{-i\omega t}dt, \tag{18}$$

where

$$C_M(t)=\left\langle\sum_{i=1}^{N} m_i\mathbf{v}_i(0)\mathbf{v}_i(t)\right\rangle, \tag{19}$$

and the averaging is done over several ensembles.

Owing to the ergodic hypothesis, time averaging is done rather than ensemble averaging. When calculating the Fourier transform, we mirror[32] the autocorrelation function

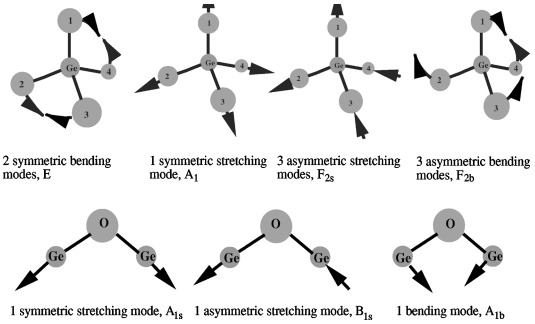

FIG. 1. Symmetry modes used for the normal-mode projections.

around $t=0$ for negative time. This is to avoid spurious high-frequency noise from the Fourier transform arising from the fact that $C_M(0)\neq 0$ and because $C_M(t)$ has only been defined for positive time.

D. Selective molecular-dynamics simulation

It is worth examining the validity of the harmonic approximation to the potential energy minimum in some detail. If anharmonicity is pronounced, the noninteracting normal-mode vibrational picture will no longer hold true. Instead modes will have finite lifetimes and their frequencies may be shifted as well. When anharmonicity is present, it is to some extent possible, however, to elucidate which are the normal modes that interact with each other by performing a constrained or *selective* molecular-dynamics simulation. We define a selective molecular-dynamics simulation to be a molecular-dynamics simulation where we preclude certain normal-mode vibrations from occurring during the course of a molecular-dynamics simulation; i.e., we make a projection of the configuration displacement, the velocities and accelerations on to the subspace of allowed displacement vectors. Exactly what integration algorithm is employed in the molecular-dynamics simulation is not important. Here we describe our method with the velocity-Verlet algorithm. The traditional velocity-Verlet algorithm used in molecular dynamics for integrating the equations of motions reads as follows:

$$\mathbf{r}(t+\delta t)=\mathbf{r}(t)+\delta t\mathbf{v}(t)+\frac{1}{2}\delta t^2\mathbf{a}(t), \tag{20}$$

$$\mathbf{v}(t+\delta t)=\mathbf{v}(t)+\frac{1}{2}\delta t[\mathbf{a}(t)+\mathbf{a}(t+\delta t)]. \tag{21}$$

Here $\mathbf{r}(t)$ is the configuration vector containing the coordinates of all the atoms, $\mathbf{v}(t)$ is the configurational velocity vector, and $\mathbf{a}(t)$ is the configurational acceleration vector. We modify the algorithm to read as follows:

$$\mathbf{r}(t+\delta t)=\mathbf{r}(t)+\delta t\hat{\mathbf{P}}_M\mathbf{v}(t)+\frac{1}{2}\delta t^2\hat{\mathbf{P}}_\mathbf{M}\mathbf{a}(t), \tag{22}$$

$$\mathbf{v}(t+\delta t)=\hat{\mathbf{P}}_M\left(\mathbf{v}(t)+\frac{1}{2}\delta t[\mathbf{a}(t)+\mathbf{a}(t+\delta t)]\right), \tag{23}$$

where $\hat{\mathbf{P}}_M$ is the projection operator that projects $\mathbf{v}$ and $\mathbf{a}$ onto the subspace of allowed normal-mode vibrations denoted by the set M. The normal modes are, as usual, obtained from diagonalizing the Hessian after a zero-Kelvin structure optimization of the system.

When omitting the normal modes $\bar{M}$ from the $3N$ normal modes, N being the number of atoms, we also adjust the thermostat applied in the molecular-dynamics program to take into account the fewer degrees of freedom. Although the system loses the degrees of freedom contained in the set $\bar{M}$, there is no physical constraint preventing the system from vibrating at an arbitrary frequency, say a frequency corresponding to one of the precluded modes. A detailed account of the selective molecular-dynamics simulation will be reported elsewhere.

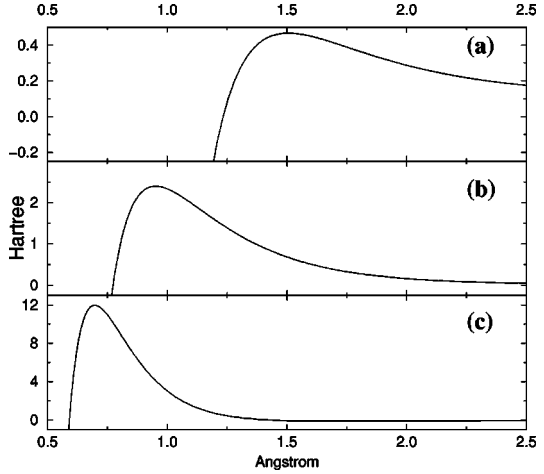

FIG. 2. (a) $V_{\mathrm{OO}}^{\mathrm{Tsuneyuki}}(r)$, (b) $V_{\mathrm{OO}}(r)$, and (c) $V_{\mathrm{GeO}}(r)$.

IV. DYNAMICAL INFORMATION AIDING THE CHOICE OF POTENTIAL

Experimentally three frequency bands for vibrations in α-quartz GeO_2 are found:[35] an upper limit of the low-frequency band at 332 cm^{-1}, a medium-frequency band between 442 and 595 cm^{-1} and a high-frequency band between 857 and 970 cm^{-1}. Preliminary calculations of the VDOS for the original potential obtained from the fitting algorithm predicted too high frequencies for all of the three frequency bands found for α-quartz GeO_2. For this instance, the upper limit of the high-frequency band was found to be 1545 cm^{-1}. However, the relative positions of the frequency bands were good. Therefore we rescaled the potential from $V(r_{ij})$ to $U(r_{ij})=c\cdot V(r_{ij})$. In the harmonic approximation we would then have $\mathrm{VDOS}_U(\sqrt{c}\cdot\omega)=\mathrm{VDOS}_V(\omega)$. With the maximum frequency being 1545 cm^{-1} this yields a scale factor of $c=(970/1545)^2=0.394$. This rescaled potential is therefore the one used throughout this paper and all results were obtained with it. The potential therefore predicts the vibrational spectra of α-quartz GeO_2 quite well but not necessarily the spectra of rutilelike GeO_2. We therefore analyze the α-quartz GeO_2 spectra in greater detail than the rutilelike GeO_2 spectra. The preliminary calculations of the VDOS were done at constant volume. As the simulation cell may change volume slightly under constant pressure the predicted frequencies may also change slightly.

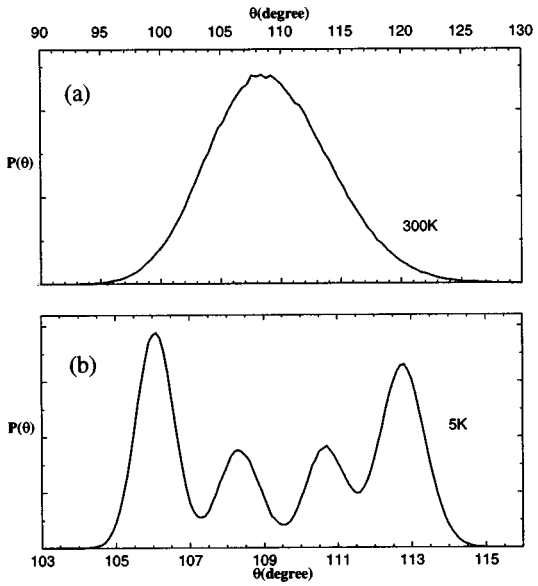

FIG. 3. The O-Ge-O angular distribution function of α-quartz GeO_2 at (a) 300 K and (b) 5 K.

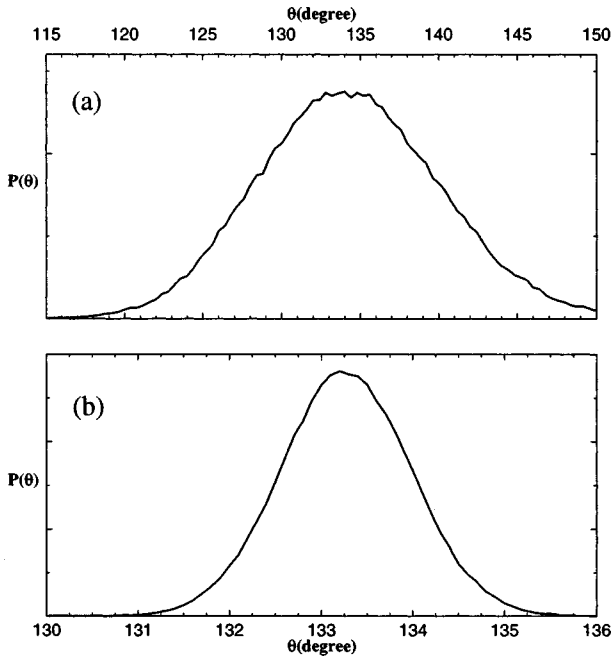

FIG. 4. The Ge-O-Ge angular distribution function of α-quartz GeO_2 at (a) 300 K and (b) 5 K.

Caution must be exercised before applying a pair potential. If the attractive C_{ij}/r^6 terms are large they will overwhelm the short-range repulsion at atomic separation distances that could be attained at high temperatures. If this is the case, the parameters must be corrected by introducing repulsive terms that fall off faster than $1/r^6$. This has been necessary to do for the Tsuneyuki potential for silica[36] but should not be necessary for our potential. In Fig. 2 we compare $V_{OO}(r)$ with $V_{OO}^{Tsuneyuki}(r)$. It is seen that it is unlikely that the short-range repulsion will be overwhelmed by the C_{OO}/r^6 term since this barrier is an order of magnitude greater than for $V_{OO}^{Tsuneyuki}(r)$. This also applies for $V_{GeO}(r)$.

V. RESULTS

A. Static structure

Figure 3(a) shows that in the simulation performed at 300 K, the O-Ge-O bond angle distribution is very broad and featureless. However, the corresponding function for the 5 K simulation, Fig. 3(b), clearly shows four distinct preferred angles whose values correspond with the ones given in Table II calculated from the fractional coordinates. That they do not agree completely is probably due to the crystal being thermally contracted in the 5 K simulation. It is interesting to

TABLE II. Structural parameters for α-quartz GeO_2 obtained from the 300 K simulation compared with experimental values.

	This work			Experiment Ref. 37	
P/GPa	0	0.5	3.55	0.0001	3.55
a,b/Å	5.130	5.078	4.854	4.9858	4.8546
c/Å	5.7378	5.7264	5.6793	5.6473	5.5943
c/a	1.118	1.127	1.170	1.1327	1.1422
ρ/(kg/m^3)	3984.4	4074.14	4496.9	4286.5	4564.2
r_{GeO}/Å	1.746	1.743	1.7405	1.737	1.729
	1.749	1.747	1.7451	1.742	1.738
Δr_{GeO}/Å	0.1		0.0982		
$\angle_{GeOGe}$	135.1°	133.6°	127.3°	129.89°	126.14
$\Delta\angle_{GeOGe}$	11°		8.7°		
$\angle_{OGeO}$	106.6°	106.1°	103.9°	106.3° [a]	105.4
	108.5°	108.3°	106.8°	107.2°	106.5
	110.9°	110.7°	109.0°	110.3°	111.9
	112.0°	112.7°	116.8°	113.5° [a]	113.9
Cell volume/Å^3	130.79	127.91	115.88	121.57	114.18
Energy/(kJ/mol)	−1283.5				

[a]Angle occurs twice in the tetrahedron.

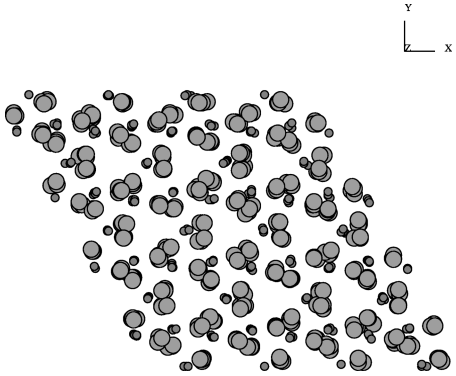

FIG. 5. Snapshot along the c axis of the simulation cell with $4\times4\times4$ α-quartz GeO_2 unit cells equilibrated at 300 K. Large spheres, O, smaller spheres, Ge.

see that the peaks in the O-Ge-O bond angle distribution in Fig. 3(b) at 106.6° and 112.0° obtained in this work correspond very well to the angles at 106.3° and 113.5° found experimentally. Reference 37 states that each of these two angles occur twice per tetrahedron whereas the two other angles at 108.5° and 110.9°, corresponding to the experimental angles 107.2° and 110.3°, occur only once for each tetrahedron. The intensity of the peaks in Fig. 3(b) confirms this fact. The Ge-O-Ge angular distribution shown in Fig. 4 peaks at $\simeq$135°, in good agreement with experiment.

The comparisons of experimental observations with our calculations are given in Tables II and III and show good agreement with experiments. Snapshots of the equilibrated α-quartz GeO_2 and rutilelike GeO_2 structures are shown in Figs. 5 and 6, respectively. The calculations of the angles and bond lengths have been facilitated by calculating the time-averaged fractional coordinates of the atoms from the MD simulations. This enables the exact average bond lengths and bond angles to be determined and confirms that two distinct Ge-O bond lengths exist as well as four distinct tetrahedral angles. The exact bond lengths cannot be determined from the pair-correlation functions as the difference between the bond lengths is much less than the thermal average variation of the bonds given above. This is also the case for the tetrahedral angles, see Table II.

For the α-quartz GeO_2 structure at zero pressure, the potential predicts bond angles and bond lengths in good agreement with experiment. It is also apparent that at elevated pressure mainly the intertetrahedral Ge-O-Ge angle changes whereas the tetrahedral angles only change very little. The unit-cell parameters, and hence the density, are also in reasonable agreement with experiment although the unit-cell vectors are 2% too large on average.

TABLE III. Structural parameters for rutilelike GeO_2 obtained from the 300 K simulation compared with experimental values.

	This work	Experiment Ref. 37
P/GPa	0	0.0001
a,b/Å	4.5623	4.4066
c/Å	2.7474	2.8619
c/a	0.6021	0.6494
ρ/(kg/m^3)	6306.5	6251.7
Oxygen position	0.30319	0.30604
r_{GeO}/Å	1.870	1.874
	1.957	1.906
Cell volume/Å^3	57.27	55.573
Energy/(kJ/mol)	−1285.3	

Elasticity

A property like the bulk modulus, $B=-V\partial P/\partial V$, may in certain simple cases, e.g., a monatomic fcc-lattice crystal, be calculated from direct analytical derivations of a pair potential, provided the volume change is isotropic. Experiments[37–39] show this is not the case for α-quartz GeO_2 where it is the changes in the tilt angle of GeO_4 tetrahedra that to a considerable extent are responsible for the shrinkage of the volume of the unit cell under pressure. Hence, an analytical estimate of the bulk modulus would not be straightforward. Thus, although it would be the most rigorous way of obtaining B, we rather derive B directly from simulations done at elevated pressures at 0.5 GPa.

As above, with the aid of average fractional coordinates, the exact bond lengths and bond angles were determined. The results shown in Table II predict that the unit cell subject to pressure contracts anisotropically, less along the c axis than along the a,b axes. The GeO bond lengths change less than do the GeGe distances, as the pressure is raised. Likewise, none of the angles remain constant as the pressure is elevated, in particular not the Ge-O-Ge angle. This indicates that compressing α-quartz GeO_2 results in a slight rotation of the GeO_4 tetrahedra rather than a volume decrease of the tetrahedra, in agreement with experiments. From the cell volume at 0.5 and 0 GPa the bulk modulus was found to be $B=22.71$ GPa. This is somewhat small when compared to the

TABLE IV. Elastic constants for the α-quartz and the rutilelike GeO_2 structures.

C_{ij}/GPa	Quartz			Rutile		
	Experiment (Ref. 47)	This work	Tsuchiya (Ref. 19)	Experiment (Ref. 48)	This work	Tsuchiya (Ref. 19)
C_{11}	64	47.0	125	337.2	300	492
C_{12}	22	15.8	46	188.2	97	238
C_{13}	32	18.9	56	187.4	143	239
C_{14}	2	−0.54	−8			
C_{33}	118	94.3	234	599.4	474	679
C_{44}	37	26.4	57	161.5	150	197
C_{66}	21	15.6	39	258.4	93	165

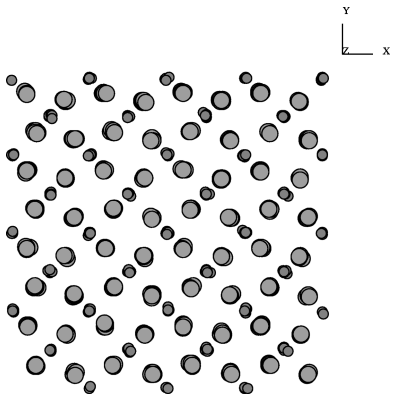

FIG. 6. Snapshot along the c axis of the simulation cell with $4\times4\times7$ rutilelike GeO_2 unit cells equilibrated at 300 K. Large spheres, O, smaller spheres, Ge.

experimental[38,39] values $B=39.2$ GPa and $B=39.1$ GPa.

The elastic constants were calculated using the program GULP.[40] For comparison we also calculated the elastic constants using the potential given in Ref. 19, see Table IV. One could anticipate that the potential proposed by Tsuchiya *et al.* would reproduce the elastic constants quite well since they have also optimized it to the bulk moduli of the two structures. However for α-quartz GeO_2, the elastic constants calculated using their potential are almost all too large by about a factor 2. In contrast our potential predicts elastic constants that are somewhat closer to the experimental values, underestimating them at most by 30%. The elastic constants predicted by our potential for the rutilelike GeO_2 structure are too small by about 30% on average, whereas the constants predicted by Tsuchiya *et al.* are overestimated by about 20%. Both potentials however fail to predict the shear-elastic constant C_{66} for rutilelike GeO_2.

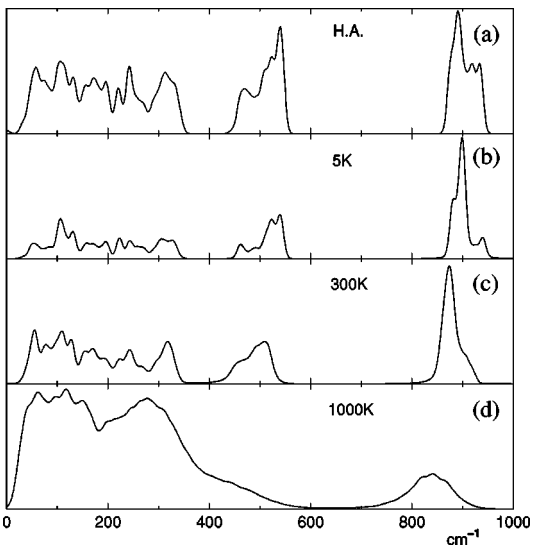

FIG. 7. Vibrational density of states for α-quartz GeO_2 obtained from (a) harmonic approximation and (b,c,d) power spectra of velocity autocorrelation function obtained from 5, 300, and 1000 K molecular-dynamics simulations, respectively. The VDOS scales are not the same in each case.

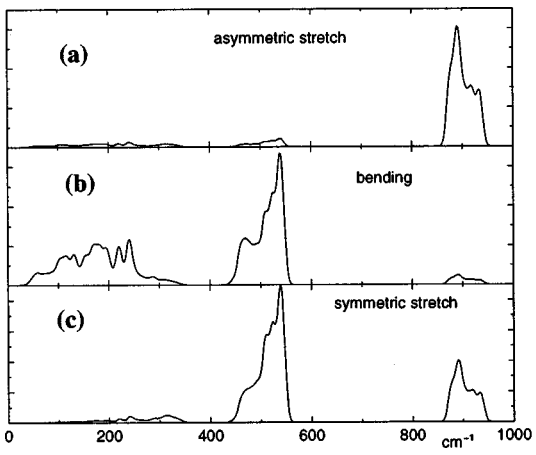

FIG. 8. Projection of normal modes onto symmetry modes for GeOGe units for α-quartz GeO_2.

B. Dynamics for α-quartz GeO_2

The frequency bands for the α-quartz GeO_2 VDOS agree very well with experiments.[35] We find the following frequency bands: an upper limit of the low-frequency band at 345 cm^{-1}, a medium-frequency band between 446 and 547 cm^{-1} and a high-frequency band between 870 and 942 cm^{-1}, as shown in Fig. 7.

The Ge-O-Ge mode analysis displayed in Fig. 8 shows that bending and symmetric stretching are responsible for the medium-frequency band, while asymmetric-stretch vibrations dominate the high-frequency band.

The mode analysis for the tetrahedra (Fig. 9) predicts that the asymmetric stretch is responsible for the peak at 890 cm^{-1}. Asymmetric and symmetric bending is mostly confined to the medium-frequency band and the low-frequency band. The symmetric-stretch vibration is responsible for the peak in the high-frequency band at 942 cm^{-1}. The rotational modes of the tetrahedra are mostly present in the low-frequency and the medium-frequency band.

The calculated Raman spectrum shown in Fig. 10(b) agrees very well with experimental observations.[35,41,42] The pronounced peak at 445 cm^{-1} is in remarkably good agreement with experiments[41] that report this peak to be at 443 cm^{-1}. The modes are tabulated in Table V where we have

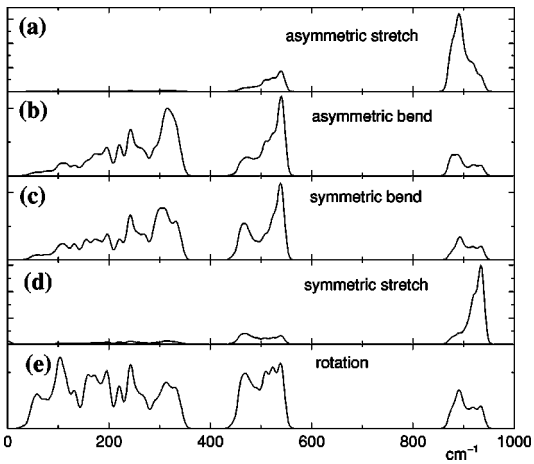

FIG. 9. Projection of normal modes onto symmetry modes of GeO_4 tetrahedra for α-quartz GeO_2.

TABLE V. Raman and infrared modes for α-quartz GeO_2 calculated within the harmonic approximation, compared with experiment. Wave numbers in bold indicate a strong intensity.

Raman cm^{-1}		Infrared cm^{-1}	
This work	Ref. 41	This work	Ref. 35
937		933	958
895		**897**	**886**
875		**876**	
800			
540	583	540	584
		520	554
493	516	**493**	518
445	**443**		
333		**333**	**332**
296		274	
200		**240**	212
175		200	
147		175	
103			

tentatively associated the modes we calculate with the corresponding experimental ones. For the harmonic approximation of the IR spectrum in Fig. 10(a), both the intensities of the spectrum and the location of the peak frequencies are in very good agreement with experiments.[35]

If we compare the Raman spectrum with the mode analysis in Figs. 8 and 9, we note that the intense mode at 443 cm^{-1} can be ascribed to symmetric-stretching and bending vibrations of Ge-O-Ge units, as well as rotations, symmetric, and asymmetric bending of GeO_4 units. This suggests that this mode is a breathing mode of a larger structure of GeO_4 tetrahedra. This conjecture is supported by Ref. 42 which reports that this Raman band is due to symmetric stretching of six-membered rings of GeO_4 tetrahedra.

Now we turn to a comparison of the vibrational density of states calculated during a molecular-dynamics simulation and the one predicted by the harmonic approximation. Looking at the VDOS in Fig. 7, we find that the low-temperature VDOS at 5 K agrees well with the VDOS predicted by the harmonic approximation. All prominent peaks in Fig. 7(a) are present in Fig. 7(b) and the intensities all agree quite well. However, the 300 K simulation shows a significant difference. Although the main peaks are present, their features have to some extent been washed out. This is especially

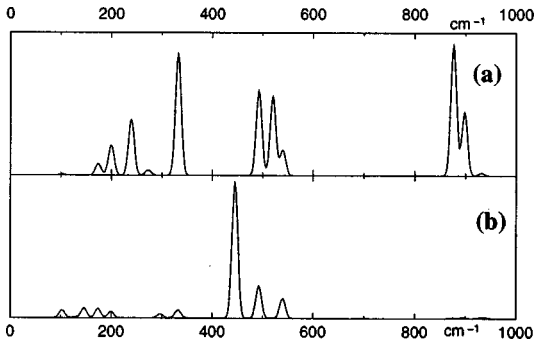

FIG. 10. Infrared (a) and Raman (b) spectra obtained in the harmonic approximation.

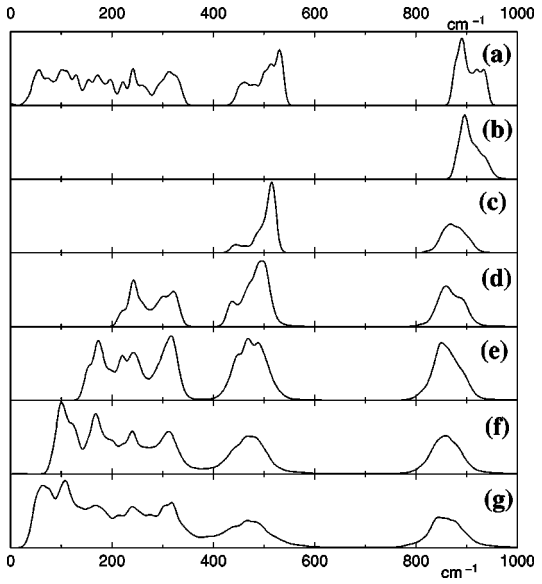

FIG. 11. VDOS for α-quartz GeO_2, (a) in the harmonic approximation and from selective MD simulations precluding frequencies lower than 870 cm^{-1} (b), 436 cm^{-1} (c), 209 cm^{-1} (d), 140 cm^{-1} (e), 77 cm^{-1} (f), and 0 cm^{-1} (g). The VDOS scales are not the same in each case.

the case for the high-frequency band (>870 cm^{-1}) which, besides being attenuated, exhibits a slight downward shift in position. The 1000 K simulation shows an even more drastic attenuation, the higher the frequency. These observations correspond to similar ones made experimentally for the Raman spectra,[41] where it was found that already at room temperature high-frequency modes are washed out and can only be resolved properly at temperatures below 109 K.

We then did six selective molecular-dynamics simulations on α-quartz GeO_2 at 1000 K where the allowed eigenmodes were chosen to correspond to frequencies above 870, 436, 209, 140, 77, and 0 cm^{-1}, respectively. This corresponds to precluding the medium- and low-frequency bands in the first simulation and to gradually including more low-frequency modes in the subsequent simulations.

The result is shown in Fig. 11. We note that when precluding all other vibrational modes but the high-frequency band, this band retains a shape very much like the corresponding one in the harmonic approximation. The peak positions are also at their original ''harmonic'' values in Fig. 11(b). But when the medium-frequency band is included, Fig. 11(c), it is obvious that the high-frequency band has been shifted down by some 30 cm^{-1}. As more low-frequency modes are included in the simulations, Figs. 11(d)–11(g), the high-frequency and the medium-frequency bands become increasingly broad, i.e., the broadening occurs as more low-frequency modes are included in the selective MD simulations.

Similar selective MD simulations on α-quartz SiO_2 using the Tsuneyuki potential[4] were also made. This was done to establish whether the observed features described above are present in other systems. The result is shown in Fig. 12. The 300 K VDOS from the normal MD simulation agrees very nicely with the harmonic-approximation VDOS, indicating that the anharmonicity described above is not significant at 300 K for α-quartz SiO_2. At 1200 K, however, the attenua-

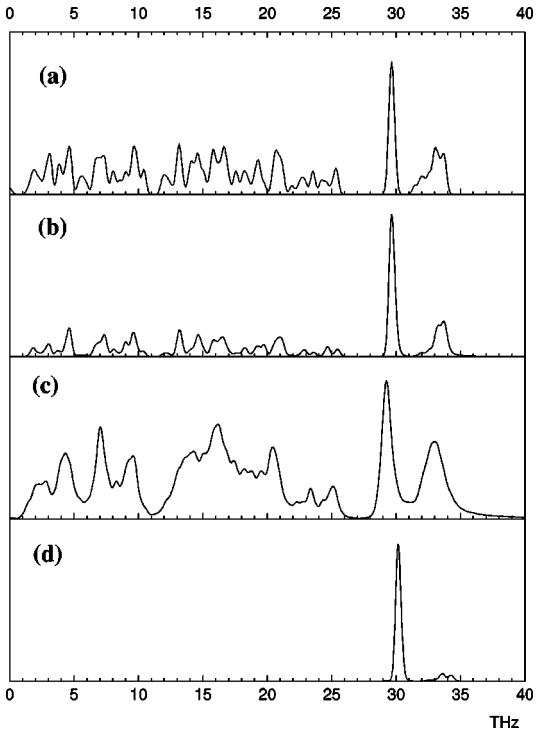

FIG. 12. VDOS for α-quartz SiO_2 in the harmonic approximation (a), extracted from the velocity autocorrelation function in a MD simulation at 300 K (b) and 1200 K (c), extracted from the velocity autocorrelation function in a MD simulation at 1200 K with the low-frequency normal modes precluded (d). The VDOS scales are not the same in each case.

tion, blurring, and downward shift of the high-frequency peaks appear. As before, the selective MD simulation shows that the high-frequency modes retain most of their features when precluding the low-frequency normal modes.

Now we will demonstrate the presence of the $\alpha-\beta$-quartz phase transition in our simulation. As has been shown,[17,43] the soft-mode phase transition from the α- to the β-quartz phase for silica occurring at 850 K for the Tsuneyuki potential is attributed to two phenomena. One is the thermal expansion of the unit cell, which lowers the double-well barrier separating the two Dauphiné twins of α quartz from each other. The other reason is the temperature itself; at high temperature the hopping over the double well from domains of one twin to a configuration identical to the other twin is easier. These workers conclude that the β-quartz phase is realized as a time average over the domains of the two twins hopping back and forth to the other twin.

We therefore carried out a series of MD calculations for α-quartz GeO_2 so as to search for any phase transition, the details of which are given in the Appendix. The temperature was varied from 100 to 2000 K with temperature steps being 50 and 25 K using the small steps near the phase transition. The fractional coordinates of the cations in α quartz can be described with the parameter u and with $1-u$ for the other α quartz twin. In β quartz, however, $u=0.5$. Thus β quartz can be regarded as a special case of α quartz and u can therefore be used as an order parameter measuring the ''α-quartz''-ness of the system. The plot of $\langle u \rangle$ versus the temperature, in Fig. 13 clearly indicates that the phase transition occurs at about 850 K. This is, however, lower than the experimental value of 1020 °C.

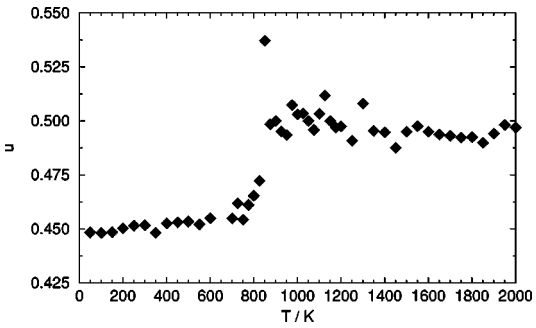

FIG. 13. Plot of the special position $\langle u \rangle$ versus temperature for the Ge atom illustrating a phase transition between α and β quartz phases of GeO_2.

C. Dynamics for rutilelike GeO_2

The vibrational spectra for the rutilelike GeO_2 structure are given in Fig. 14. As stated in Ref. 35, the experimental VDOS covers the frequency range up to 873 cm^{-1}. The VDOS calculated in Fig. 14(a) ranges up to 856 cm^{-1}. The IR and the Raman spectra are however not in perfect agreement with experiment.[35,41] The intense Raman mode observed experimentally at 700 cm^{-1} is calculated to be at 532 cm^{-1}. The broad infrared band between 300 and 700 cm^{-1} reported in experiment is not quite reproduced either in our calculations. Instead three intense frequencies are observed at 182, 347, and 414 cm^{-1}.

VI. CONCLUSION

A two-body potential, derived from fitting to the potential energy surface obtained from a Hartree-Fock calculation for a GeO_4 cluster, has proved to stabilize both crystalline phases of GeO_2 (α quartz and rutilelike) in constant-pressure, constant-temperature molecular dynamics.

As mentioned in the Introduction, pair potentials are

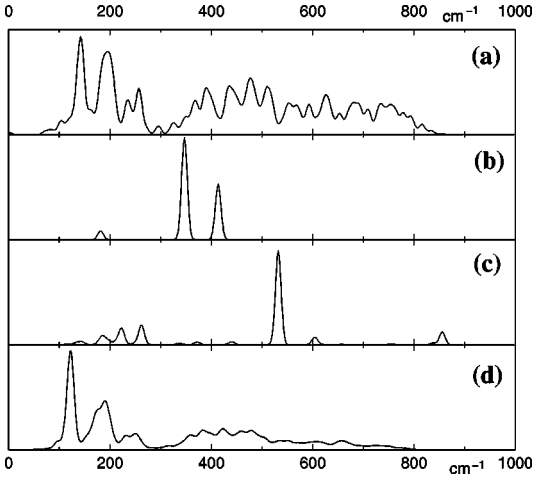

FIG. 14. VDOS in the harmonic approximation (a), IR spectrum (b), Raman spectrum (c), and power spectra of velocity autocorrelation function for rutilelike GeO_2 at 300 K. The VDOS scales are not the same in each case.

likely not to be the best functional form when modeling covalent solids. In this context it is worth stressing that none of the potential parameters therefore can be claimed to be identified with any physical property of the bulk phase, a situation which has been stated previously.[44]

The bulk modulus of α-quartz GeO_2 is in reasonable agreement with the experimental value and it is encouraging to observe that the model presented here can also account for the tilting of the GeO_4 tetrahedra in the α-quartz structure when pressure is applied. We note that the bulk modulus and the elastic constants are overall too small in our model. This could be remedied by another rescaling of the potential if these were the properties of interest. But then the VDOS would be out of the experimentally observed frequency range. This merely illustrates the limit of pair potentials.

Taking into account that the high-frequency bands are mainly associated with bond length displacements while low-frequency bands are associated with rotations and bending modes, we can therefore state that a compression of the unit cell does not significantly involve contraction of bonds in this model.

The model successfully predicted the $\alpha-\beta$ quartz phase transition, although the transition temperature is 443 degrees too low. As discussed by Smirnov,[43] the transition temperature is very sensitive to the pressure at which the simulations are carried out. A slightly higher pressure would be expected to push the transition temperature upwards, although we have not verified this.

The vibrational spectra for α-quartz GeO_2 show excellent agreement with experimental observations. The attenuation and broadening of peaks in the VDOS from MD simulations at elevated temperatures have been attributed to the anharmonicity of α-quartz GeO_2 which we have shown is more pronounced than in α-quartz SiO_2.

We observe that the validity of the harmonic approximation must be examined before inferring the VDOS from the harmonic approximation. A simulation done far away from the melting point of a particular model does not necessarily validate properties calculated within the harmonic approximation.

In the quest for a more general potential model for germania, capable of reproducing the spectra of both crystalline phases, the potential presented here may perhaps serve as a starting point. This model would possibly have to be implemented as a pair or cluster functional,[45] rather than as a many-body potential as discussed above.

ACKNOWLEDGMENTS

Thanks are due to Dr. S. N. Taraskin for valuable discussions and suggestions on the manuscript, to Professor A. D. Buckingham for useful discussions concerning the bond polarizability model, and to Professor J. P. Hansen for help with autocorrelation functions. R.D.O. is grateful for financial support from the Carlsberg Foundation.

APPENDIX

For the molecular-dynamics simulations on α-quartz GeO_2, the simulation time was set to 60 ps and data acquisition was done typically in the last 10 ps. The relaxation times for the thermostat and the barostat were of the order of 1 ps. The constant-pressure, constant-temperature simulations were implemented with the Berendsen[46] thermostat and anisotropic barostat.

For the α-quartz GeO_2 simulations, we used an Ewald-convergence parameter of 0.384 99 Å^{-1} and the number of Ewald k vectors was set to 8, 8, and 9 along the respective reciprocal simulation cell vectors. The simulation cell consisted of $4\times4\times4$ unit cells with $r_{\text{cutoff}}=8.4$ Å.

For the rutilelike GeO_2 simulations, we used an Ewald-convergence parameter of 0.384 99 Å^{-1} and the number of Ewald k vectors was set to 7, 7, and 9 along the respective reciprocal simulation cell vectors. The simulation cell consisted of $4\times4\times7$ unit cells with $r_{\text{cutoff}}=8.4$ Å.

For the spectra in the harmonic approximation, the system set up for the IR, Raman, VDOS, and mode-projection spectra was as for the molecular-dynamics simulations. The system was then relaxed at zero pressure using the anisotropic barostat until the forces on any of the atoms were no greater than 3.0×10^{-11} N and the components of the pressure tensor were no greater than 0.3 kbar.

For the selective molecular-dynamics simulation, the system setup was as for the α-quartz GeO_2 MD simulations but the runs were shortened to only 7 ps with 3 ps equilibration time.

For the simulations of the $\alpha-\beta$ quartz phase transition, the simulation cell consisted of $3\times3\times3$ unit cells, an Ewald-convergence parameter of 0.5472 Å^{-1}, the number of Ewald k vectors set to 8, 8, and 9 and the thermostat and barostat relaxation times as above. The total simulation time was set to 40 ps with equilibration during the first 30 ps. The calculations were done on Silicon Graphics workstations equipped with R8000 processors running at 75 MHz and R10000 processors running at 194 MHz.

[1] A. Takada *et al.*, Phys. Rev. B **51**, 1447 (1995).
[2] R. Nada, C. R. A. Catlow, R. Dovesi, and C. Pisani, Phys. Chem. Miner. **17**, 353 (1990).
[3] R. Car and M. Parrinello, Phys. Rev. Lett. **55**, 2471 (1985).
[4] S. Tsuneyuki, M. Tsukada, H. Aoki, and Y. Matsui, Phys. Rev. Lett. **61**, 869 (1988).
[5] A. Lasaga and G. V. Gibbs, Phys. Chem. Miner. **14**, 107 (1987).
[6] M. J. L. Sangster and M. Dixon, Adv. Phys. **1976**, 247 (1976).
[7] F. G. Fumi and M. P. Tosi, J. Phys. Chem. Solids **25**, 31 (1964).
[8] A. P. Sutton and J. Chen, Philos. Mag. Lett. **61**, 139 (1990).
[9] V. Heine, I. J. Robertson, and M. C. Payne, Philos. Trans. R. Soc. London, Ser. A **334**, 393 (1991).
[10] A. E. Carlsson, J. C. D. Gelatt, and H. Ehrenreich, Philos. Mag. A **41**, 241 (1980).
[11] M. Z. Bazant and E. Kaxiras, Phys. Rev. Lett. **77**, 4370 (1996).
[12] F. H. Stillinger and T. A. Weber, Phys. Rev. B **31**, 5262 (1985).
[13] B. W. H. van Beest, G. J. Kramer, and R. A. van Santen, Phys. Rev. Lett. **64**, 1955 (1990).
[14] A. W. Laubengayer and D. S. Morton, J. Am. Chem. Soc. **54**, 2303 (1932).

[15] J. S. Tse and D. D. Klug, J. Chem. Phys. **95**, 9176 (1991).
[16] I. Etxebarria, R. M. Lynden-Bell, and J. M. Perez-Mato, Phys. Rev. B **46**, 13 687 (1992).
[17] S. Tsuneyuki, H. Aoki, M. Tsukada, and Y. Matsui, Phys. Rev. Lett. **64**, 776 (1990).
[18] A. R. George and C. R. A. Catlow, J. Solid State Chem. **127**, 137 (1996).
[19] T. Tsuchiya, T. Yamanak, and M. Matsui, Phys. Chem. Miner. **25**, 94 (1998).
[20] M. C. Payne, I. J. Robertson, D. Thomson, and V. Heine, Philos. Mag. B **73**, 191 (1996).
[21] R. D. Amos *et al.*, CADPAC6.0, *The Cambridge Analytical Derivatives Package*, University of Cambridge, CB2 1EW, England, 1995.
[22] A. Szabo and N. S. Ostlund, *Modern Quantum Chemistry*, 1st ed. (McGraw-Hill, New York, 1989).
[23] W. H. Press, S. A. Teukolsky, W. T. Vetterling, and B. P. Flannering, *Numerical Recipes in C*, 2nd ed. (Cambridge University Press, Cambridge, 1992).
[24] D. A. Kleinman and W. G. Spitzer, Phys. Rev. **125**, 16 (1962).
[25] A. J. M. de Man, B. W. H. van Beest, M. Leslie, and R. A. van Santen, J. Phys. Chem. **94**, 2524 (1990).
[26] D. A. Long, Proc. Phys. Soc. London, Sect. A **217a**, 203 (1953).
[27] J. A. Creighton, H. W. Deckman, and J. M. Newsam, J. Phys. Chem. **98**, 448 (1994).
[28] Basis sets were obtained from the Extensible Computational Chemistry Environment Basis Set Database, Version 1.0, as developed and distributed by the Molecular Science Computing Facility, Environmental and Molecular Sciences Laboratory which is part of the Pacific Northwest Laboratory, P.O. Box 999, Richland, Washington 99352, and funded by the U.S. Department of Energy. The Pacific Northwest Laboratory is a multiprogram laboratory operated by Battelle Memorial Institute for the U.S. Department of Energy under Contract No. DE-AC06-76RLO 1830. Contact David Feller, Karen Schuchardt, or Don Jones for further information.
[29] S. N. Taraskin and S. R. Elliott, Phys. Rev. B **56**, 8605 (1997).
[30] M. Wilson, P. A. Madden, M. Hemmati, and C. A. Angell, Phys. Rev. Lett. **77**, 4023 (1996).
[31] J. M. Dickey and A. Paskin, Phys. Rev. **188**, 1407 (1969).
[32] B. Winkler and M. T. Dove, Phys. Chem. Miner. **18**, 407 (1992).
[33] R. G. D. Valle and E. Venuti, Chem. Phys. **179**, 411 (1994).
[34] B. Boulard, J. Kieffer, C. C. Phifer, and C. A. Angell, J. Non-Cryst. Solids **140**, 350 (1992).
[35] M. Madon, P. Gillet, C. Julien, and G. D. Price, Phys. Chem. Miner. **18**, 7 (1991).
[36] Y. Guissani and B. Guillot, J. Phys. Chem. **104**, 7633 (1996).
[37] T. Yamanaka and K. Ogata, J. Appl. Crystallogr. **24**, 111 (1991).
[38] J. Glinnemann *et al.*, Z. Kristallogr. **198**, 177 (1992).
[39] J. D. Jorgensen, J. Appl. Phys. **49**, 5473 (1978).
[40] J. Gale, GULP, *General Utility Lattice Program*, Imperial College, South Kensington, London, SW7 2AY, version 1.1.
[41] T. P. Mernagh and L. gun Liu, Phys. Chem. Miner. **24**, 7 (1997).
[42] E. I. Kamitsos *et al.*, J. Phys. Chem. **100**, 11 755 (1996).
[43] M. B. Smirnov and A. P. Mirgorodsky, Phys. Rev. Lett. **78**, 2413 (1997).
[44] G. J. Kramer, N. P. Farragher, B. W. H. van Beest, and R. A. van Santen, Phys. Rev. B **43**, 5068 (1991).
[45] A. E. Carlsson, in *Solid State Physics*, edited by H. Ehrenreich and D. Turnbull (Academic, San Diego, 1990), Vol. 43, pp. 1–91.
[46] H. J. C. Berendsen *et al.*, J. Phys. Chem. **81**, 3684 (1984).
[47] M. Grimsditch, A. Polian, V. Brazkhin, and D. Balitskii, J. Appl. Phys. **83**, 3018 (1998).
[48] H. Wang and G. Simmons, J. Geophys. Res. **78**, 1262 (1973).